VII International Conference on Computational Methods for Coupled Problems in Science and Engineering
COUPLED PROBLEMS 2017
M. Papadrakakis, E. Oñate and B. Schrefler (Eds)

COUPLED NUMERICAL SIMULATION OF ANTI-ICING PROBLEMS

Emiliano Iuliano* **and Michele Ferraiuolo†**

*Italian Aerospace Research Center (CIRA)
Fluid Mechanics Department
Via Maiorise, 81043 Capua, Italy
e-mail: e.iuliano@cira.it, web page:
http://www.cira.it/it/corporate/chi-siamo/persone/dettaglio-persona?email=e.iuliano@cira.it

†Italian Aerospace Research Center (CIRA)
Thermo-structural Design Department
Via Maiorise, 81043 Capua, Italy
e-mail: m.ferraiuolo@cira.it - Web page: http://www.cira.it/it/corporate/chi-siamo/persone/dettaglio-persona?email=m.ferraiuolo@cira.it

Key words: In-flight icing, coupled approach, FEM, CFD, ice protection system

Abstract.
The paper proposes a coupled methodology able to simulate and optimize the performance of an electrothermal anti-icing system in an integrated fashion: in fact, the classical tool chain of icing simulation (aerodynamics, water catch and impact, mass and energy surface balance) is coupled to the thermal analysis through the surface substrate and the ice thickness. In general, the substrate consists of a multi-layered composite with different properties for each layer and embedded heaters (resistors) at interfaces between layers. The current practice is to size the anti-icing system by evaluating the most critical icing conditions through ice accretion simulation, verifying that no ice is formed on the surface and, finally, estimating the required heating power. In the present approach, the ice protection simulation is not decoupled from the ice accretion simulation, but a single computational work–flow is considered. Validation results obtained on benchmark test cases, drawn from NASA database, will be detailed as well as comparison with numerical results from other authors.

1 Introduction

The formation of ice on aircraft components is a severe issue for in-flight safety. Liquid water droplets may exist in supercooled conditions up to $-40°$, remaining in an unstable state until they undergo an external disturbance, e.g. the impact with an aircraft surface. Depending on the environment and surface substrate conditions, the supercooled droplets may freeze immediately upon contact, partially stick and partially being ejected off the body (splashing, rebounding), deposit and flow along the surface (runback). In case of severe ice accretion, the aerodynamics of the aircraft surface can be severely deteriorated, leading to a decrease in lift and controllability and an increase in drag. Ice protection systems (IPS) are usually designed to prevent ice accretion (anti-icing systems) or to restore clean conditions (de-icing systems). The design of reliable ice protection systems (IPS) is critical and the effectiveness of such devices are required to be thoroughly demonstrated by strict regulations (14 CFR 25.1419 by the FAA or under CS

25.1419 by EASA). Anti-icing systems act to increase the surface temperature above the freezing point, allowing the caught water mass to flow downstream (running-wet anti-icing) or to evaporate (evaporative anti-icing). De-icing systems are activated once a limited amount of ice has already accreted on the aircraft surface, decrease the adhesion forces by de-bonding the inner ice layers and let the aerodynamic forces clean up the surface by removing the detached ice fragments. The heat required by the anti-icing systems is usually provided by electrical heaters embedded within the surface metal skin (electro-thermal anti-icing) or by hot air coming from the engine bleed system and impinging on the internal surface of the metal skin (hot-air anti-icing). De-icing systems may be of different kind: mechanical (pneumatic boots), electro-thermal or electro-mechanical. In case of an anti-icing system, the region to be protected is usually larger than the water droplets impingement area in order to decrease the probability of ice formation due to runback flow.

Numerical simulation represents a crucial step towards the design process of anti-icing systems and the reduction of the experimental testing burden. In the following, a coupled approach is presented which integrates two different physics: the aero-thermodynamics on the airfoil surface, where different phenomena may occur (impingement, water film formation, freezing, evaporation, heat transfer), and the heat conduction through the airfoil skin where heater elements are properly allocated. The coupled procedure is structured in a parametric way in order to be proficiently used within an optimization process to improve the performance of the anti-icing system. The paper is structured as follows: the mathematical models are presented in the next section, then some information about the numerical method are provided and the coupling strategy is presented. The obtained results are shown and discussed in the final section.

2 Mathematical Model

2.1 Heat conduction model

The steady state heat conduction problem with heat generation inside a solid body is governed by the differential equation [15]:

$$\nabla^2 T = \frac{\partial^2 T}{\partial s^2} + \frac{\partial^2 T}{\partial n^2} = -\frac{g}{k} \tag{1}$$

where s and t are the tangential and normal to surface directions, g represents the heat generation of the electrothermal pad elements and k is the thermal conductivity. Convective boundary condition on the skin external surface are applied (see also figure 1):

$$-k_w \frac{\partial T}{\partial n} = h_{eff}(T_s - T_\infty) \tag{2}$$

where k_w is the thermal conductivity of the first layer of the skin, h_{eff} is the effective heat transfer coefficient (see also section 4), T_s is the surface temperature of the skin and T_∞ is the ambient air temperature.

Since the skin is made of several layers characterized by different thermal conductivities, temperature and heat flux continuity conditions are applied at the interface between layers i and $i+1$:

$$k_i \frac{\partial T_i}{\partial n_i} = k_{i+1} \frac{\partial T_{i+1}}{\partial n_{i+1}}$$
$$T_i = T_{i+1}$$

2.2 Messinger model for ice accretion

The pioneering work by Messinger [13] provided a simple model to describe the heat and mass balance onto a surface covered by a thin, continuous water film. In its original form, the model represents a

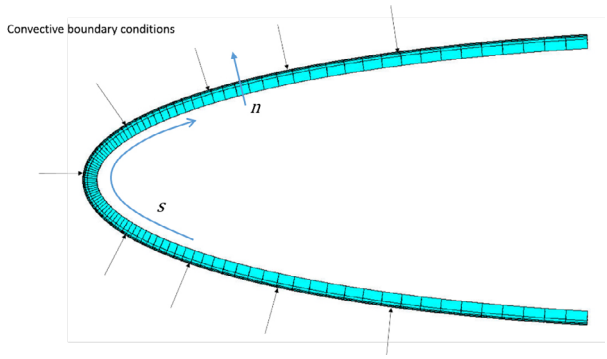

Figure 1: Curvilinear reference system and convective boundary conditions on the skin profile

one-dimensional, equilibrium energy balance to evaluate the equilibrium temperature onto an unheated, insulated surface exposed to icing. In practice, it is evaluated at discrete positions around the leading edge of the body under investigation by using a control volume approach. The calculation normally starts at the air flow stagnation point. The unknowns are the surface temperature and a parameter known as the freezing fraction, f. The latter represents the ratio of the water which freezes at a specified location with respect to the incoming water. Any unfrozen water is assumed to flow back, termed runback water, along the surface and is included in the analysis of the next downstream control volume. From the freezing fraction, the rate of ice growth may be estimated and, consequently, the ice profile can be predicted once fixed the icing time. Otherwise, the simulation of an anti-icing system is carried out by adding heat source terms.

Since the original formulation, several enhancements contributed to the improvement of the model, such as the inclusion of compressibility heating [4], the addition of an energy source from the substrate to simulate anti-icing systems [12], the simulation of conduction through the ice layer [10] an of the resulting phase change due to the heat flow [14].

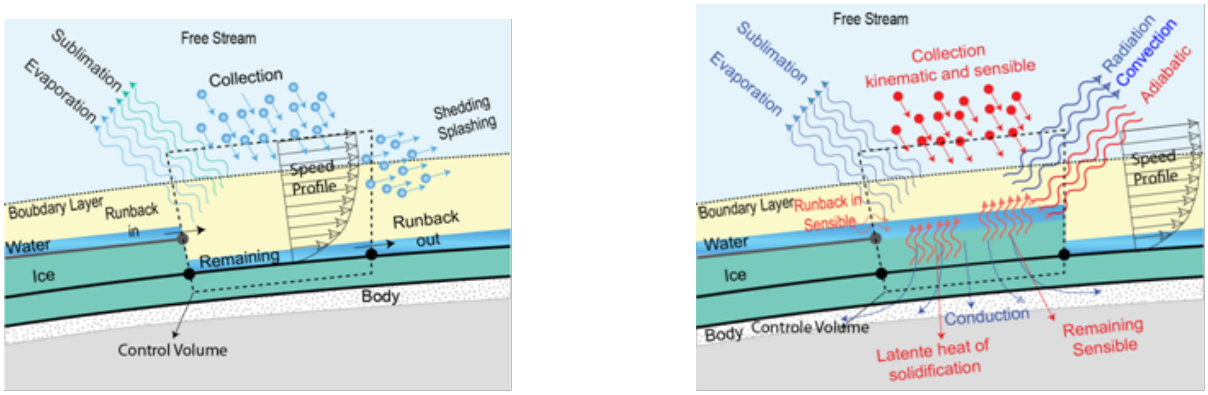

(a) Mass balance

(b) Energy balance

Figure 2: Control volume terms in Messinger model

The Messinger model is based on two main equations: the mass and energy balance on the icing surface. With reference to figure 2, the mass balance states that the water mass incoming into each

control volume cell must be equated by the outgoing water:

$$m_{in} = m_{imp} + m_{rbin} \equiv m_{out} = m_{ice} + m_{evs} + m_{rbo} \tag{3}$$

where $m_{imp} = \beta V_\infty LWC_\infty \Delta S \Delta t$ (β is the droplet collection efficiency, V_∞ is the free-stream droplet velocity and LWC_∞ is the free-stream liquid water content in Kg/m^3, ΔS is the area of the surface element of the control volume and Δt is the icing exposure time) is the impinging water mass, m_{rbin} is the runback water from the upstream cell, $m_{ice} = f m_{in}$ is the freezing water mass, m_{evs} is the mass which undergo evaporation or sublimation and m_{rbo} is the runback water flowing in the next downstream cell. The freezing fraction f can assume values between 0 and 1: a freezing fraction of 1 means that the entire amount of incoming liquid water freezes; a freezing fraction less than 1 means that there will be evaporation and/or liquid runback.

The evaporation/sublimation mass can be estimated by using the Fick's law:

$$m_{evs} = \bar{\rho} h_m (Y_{v,s} - Y_{v,e}) \Delta S \Delta t \tag{4}$$

where $\bar{\rho}$ is the density of the water/vapour mixture, h_m is the diffusive mass transfer coefficient, $Y_{v,s}$ and $Y_{v,e}$ are the water vapor mass fraction evaluated respectively on the surface and outside the boundary layer. By rearranging and exploiting the heat-mass transfer analogy, the evaporation mass can be written as [5]:

$$m_{evs} = \Big(\frac{Pr}{Sc}\Big)^{2/3} \Big(\frac{h}{C_{p,air}}\Big) \frac{M_w}{M_{air}} \Big[\frac{P_{v,s}(T_s) - P_{v,e}}{P_{air} - P_{v,s}(T_s)}\Big] \Delta S \Delta t \tag{5}$$

The water vapor mass fraction (Y_v) are related to the local saturated vapor pressure ($P_{v,s}$) and depends on the local surface temperature T_s. As a consequence, the mass balance equation has three unknowns: the freezing fraction, the surface equilibrium temperature and the outgoing runback mass. The outgoing running back water is computed once the fraction of freezing water f is known. To solve the problem, the heat balance on the surface is considered as sketched in figure 1. Several heat transer mechanisms can be identified, some of them act as heat sinks, some other as heat sources. The general form of the heat balance is epressed with the enthalpy formulation as follows:

$$Q_c + Q_{evs} + Q_f + Q_{sh} + Q_{kin} + Q_{ai} = 0 \tag{6}$$

where the single heat contributions are:

- $Q_c = h_c(T_{rec} - T_s)\Delta S \Delta t$ is the convective cooling heat due to air, h_c is the wall to boundary layer heat transfer coefficient, T_{rec} and T_s are the adiabatic recovery temperature and the surface temperature (unknown);
- $Q_{evs} = -m_{evs}[f L_s + (1-f) L_v] \Delta S \Delta t$ is the heat sink due to evaporation/sublimation, L_v and L_s are the latent heat of evaporation and sublimation;
- $Q_f = f m_{in} L_f \Delta S \Delta t$ is the heat source due to the release of latent heat of fusion (L_f) during the solidification process;
- $Q_{sh} = Q_{sh1} + Q_{sh2}$ is the sensible heat associated to the change of temperature in the control volume. In the most general case, this process can be divided in two thermodynamic sub-processes: first, the system has to be brought from the initial temperature to the freezing point; second, it has

to change its temperature from the freezing point to the equilibrium temperature. The two terms can be written as:

$$Q_{sh1} = m_{imp} C_{p,w} (T_{imp} - T_f) \Delta S \Delta t + m_{rbin} C_{p,w} (T_{rbin} - T_f) \Delta S \Delta t$$
$$Q_{sh2} = m_{in} (1 - f) C_{p,w} (T_f - T_s) \Delta S \Delta t + m_{in} f C_{p,i} (T_f - T_s) \Delta S \Delta t$$

with $C_{p,w}$ and $C_{p,i}$ the specific heat capacity of water and ice.

- $Q_{kin} = \frac{1}{2} m_{imp} U_d^2$ is the kinetic heat source due to incoming droplets;
- Q_{ai} is the heat provided by an anti-icing system. In case of an electrothermal system, it may be expressed in terms of the heat condution flux at the surface:

$$Q_{ai} = -k_w \frac{\partial T}{\partial n} \Delta S \Delta t \tag{7}$$

with k_w the thermal conductivity of the surface layer and $\frac{\partial T}{\partial n}$ the local temperature gradient in the direction normal to the surface.

The two equations are solved by identifying three domains in the (T_s, f, m_{rbo}) solution space (running wet, rime icing and glaze icing) and by iteratively checking the so-called compatibility relations associated to each of them: for instance, the runnig wet regime holds only if $T_s > T_f$, hence if at the end of the computation the value of the surface temperature is not compatible with this hypothesis, the solution is not valid and another regime must be considered. The heat balance equation is solved by using a classical Newton-Raphson method and evaluating at each iteration both the function value and its derivative with respect to the unknown variable (T_s or f, depending on the solution domain).

3 Numerical method

3.1 Heat conduction model

The finite element adopted for thermal analyses is a solid one with 8 nodes on the corners and temperature as the only degree of freedom [11]. This thermal element is linear since it is characterized by no mid-side nodes. The element size in the direction of the curvilinear abscissa of the profile has been set equal to the thickness of the outermost layer of the skin, while a an adequate spacing ratio has been chosen in order to take into account the presence of the electrothermal pad thickness which is much lower than the layer ones. The number of nodes in the layer thickness is such that the element length is the fourth part of the outermost layer thickness. Finally, the sparse matrix direct solver has been employed for the solution.

A parametric model has been designed in Ansys Parametric Design Language (APDL) able to analyze any kind of aerodynamic profile, skin layers layout and electro-thermal pad arrangement. The model has been conceived to be adopted in an optimization process where the capability to vary the location of the pads and their corresponding electric power is required. More specifically, two APDL batch files have been prepared: the first one (geometry/mesh file) needs geometric inputs such as the aerodynamic profile, the number and thickness of the skin layers, the ice profile in case of de-icing simulations and provides as main output the computational mesh; the second one (load/analysis file) contains the pads layout and the load conditions. In a parametric or optimization study, the geometry/mesh file is run only at the beginning of the process and a database file is created by the Finite element commercial code; on the other hand, the load/analysis file is run every time a thermal analysis is invoked and is fed with the surface distribution of the heat transfer coefficient: the design variables can be the location of the pads, the power-up switching sequence or their electric power.

In what follows a detailed description of the geometry/mesh file is given. As above mentioned, the inputs for this file are only geometric. The output is a database file containing the finite element model.

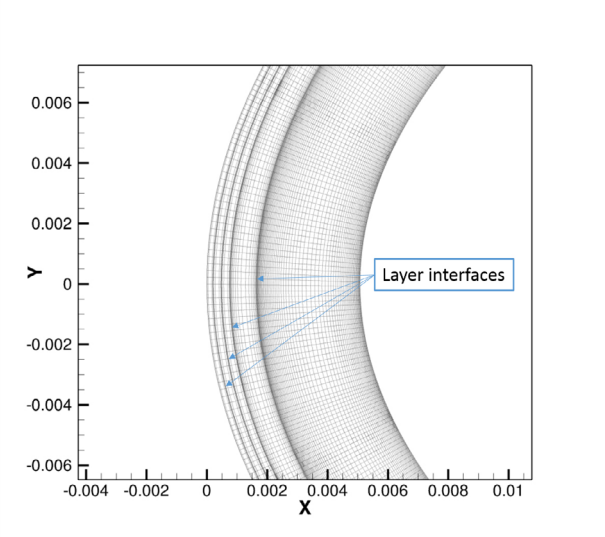

Figure 3: Example mesh in the airfoil skin with layer interfaces

The file is completely parametric and can be adopted for any kind of profile shape. Concerning the mesh generation, a specific procedure has been prepared in order to appropriately mesh the electrothermal pads whose information are given only in the second file. An example of the finite element mesh is provided in figure 3. Indeed, since the pads are supposed to be inserted between two layers and their thickness is typically very small (about 0.05 mm) if compared with the skin layers, the mesh elements are not uniformly spaced throughout the skin thickness but highly stretched in the normal to surface direction in order to have very small elements near the layer interfaces and capture the geometry of the pad elements. This is done for every layer interface as, at the time of the mesh generation, the actual location of the pads is not known yet. Such an approach gives generality to the computational process as it prevents from generating a new mesh for each thermal computation and it allows for an easy and parametric allocation of the pad elements.

In the load/analysis file, heat transfer coefficient distribution, pads power, location and activation sequence are provided. According to these data, the mesh elements which are enclosed in the specified pad region are selected and the corresponding heat power density is assigned to them. The heat transfer coefficient is included here because it represents the total (or effective) surface heat loss and in steady analyses, when a direct coupling between the finite element conduction model and the ice accretion model is realized, it may vary depending on the external conditions; in fact, as it will be described in section 4, multiple steady thermal analyses are conducted by exchanging the total heat transfer coefficient until convergence is reached.

3.2 Messinger model

The main inputs of the Messinger model are the impinging mass m_{imp} and the convective heat transfer coefficient h_c. The first is related to the collection efficiency β which, in turn, depends on the air flow and water droplet field solutions. The second depends on boundary layer characteristics. Both parameters may be computed by using various methods and approaches. Here, the air flow field is obtained by solving the Reynolds-averaged Navier-Stokes equations: to this aim, the in-house multi-block structured flow solver ZEN is used [3]. As a viscous flow solver is available, the heat transfer coefficient can be computed easily from the air flow solution as follows:

- on solid surfaces, no-slip and isothermal boundary conditions are imposed for momentum and energy

equations respectively;

- two computations are launched: the first by imposing the wall temperature $T_{w,1} = T_\infty$, the second by imposing $T_{w,2} = T_\infty - \Delta T_w$ (here $\Delta T_w = 0.5$ Kelvin). As a result, two distributions of the surface heat flux are obtained from the solutions: $\dot{q}_{w,1} = h_c(T_{w,1} - T_{rec})$ and $\dot{q}_{w,2} = h_c(T_{w,2} - T_{rec})$, where T_{rec} is the adiabatic recovery temperature. Having set the difference in wall temperature ΔT_w very small, the dependence of the convective heat transfer on the temperature can be safely neglected. Finally, having two equations with the unknowns (T_{rec}, h_c), it is possible to calculate both the recovery temperature and the heat transfer coefficient at every point of the solid surface.

As regards the collection efficiency, the in-house Eulerian solver Imp2D is employed to compute the water droplet flow field by solving PDE equations for water particles concentration $\rho_d \alpha_d$, momentum $\rho_d \alpha_d \vec{U}_d$ and energy $\rho_d \alpha_d T_d$ balance [7, 8, 6], where subscript d refers to the droplet phase. In the momentum equation, aerodynamic drag and gravity forces are introduced as source terms. The collection efficiency is computed on any solid surface as:

$$\beta = \frac{\rho_d \alpha_d (\vec{U}_d \cdot \vec{n})}{LWC_\infty U_{d,\infty}}$$

where LWC_∞ is the liquid water content of the cloud in Kg/m^3, $U_{d,\infty}$ is the free-stream droplet velocity and $\vec{n}$ is the surface normal unit vector.

Once known h_c and β distribution at any point on the solid surface, equations 3 and 6 can be solved. Given a control volume discretization of the solid surface, the procedure starts from the stagnation point, where no incoming runback mass m_{rbin} is supposed to enter and the outgoing runback mass m_{rbo} is assumed to be poured in equal parts into the adjacent control volumes; then, it proceeds downstream first on the suction side, then on the pressure side separately. For each control volume, up to three icing regimes are sequentially assumed (running wet, rime icing and glaze icing) and the related simplified equations are solved if the compatibility conditions of the former are not satisfied, as described in section 2.2.

4 Coupling approach

Equations 1,3 and 6 represent a mathematical model which has to be solved simultaneously in order to guarantee a physical solution. Moreover, a multi-zonal approach has to be employed with appropriate interface conditions: indeed, equation 1 is valid through the solid skin while equations 3 and 6 describe the physics of the external flow. The set is coupled by the surface temperature field which is an unknown in both cases. The coupling procedure is conceived to balance the total heat lost due to the external flow phenomena (evaporation, convective cooling, impingement, freezing) and the heat flux provided by the anti-icing system. The convergence metric is the effective heat transfer coefficient which is exchanged between the zonal solutions.

Here, an iterative approach is followed aiming at achieving the convergence of surface field data on both models. In other words, the heat conduction solver is iteratively fed with the Messinger model solution to realize the same heat transfer and temperature field according to some norm. The coupling procedure can be summarized as follows:

1. Initialization step: the anti-icing heat source is initialized to null and the effective heat transfer is assumed as purely convective: $Q_{ai,m} = 0$,$h_{eff,m} = h_c$;

2. Messinger model solution: equations 3 and 6 are solved and the surface temperature distribution $T_{s,m}$ is calculated;

3. Exchange parameter evaluation: the effective heat transfer coefficient is estimated by considering the total heat lost on the surface as:

$$h_{eff,hc} = \frac{1}{\Delta S \Delta t} \frac{Q_c(T_{s,m}) + Q_{evs}(T_{s,m}) + Q_f + Q_{sh}(T_{s,m}) + Q_{kin}}{T_{s,m} - T_\infty} \tag{8}$$

4. Heat conduction solution: the surface distribution of $h_{eff,hc}$ is transferred to the heat conduction solver, the temperature field T_{hc} in the solid skin is obtained by solving equation 1 with the boundary condition:

$$\dot{q}_{w,hc} = h_{eff,hc}(T_{s,hc} - T_\infty) = -k_w \frac{\partial T_{hc}}{\partial n} \tag{9}$$

where $T_{s,hc}$ is the new value of the surface temperature;

5. Convergence check: if $\|h_{eff,hc} - h_{eff,m}\|_p < \epsilon$, convergence is assumed and the solution of the coupled problem is found. Otherwise, $h_{eff,m} = h_{eff,hc}$, $Q_{ai,m} = \dot{q}_{w,hc} \Delta S \Delta t$ and one more iterative step is performed going back to point 2. Here, both $p = 2$ and $p = \infty$ are used.

The effective film coefficient h_{eff} is used for estimating the convergence of the coupled problem while a natural choice could have led to use the surface temperature T_s: however, as ice–water phase change may occur in some regions and this could keep the temperature predicted by the Messinger model fixed at the freezing point, a bias would be introduced in those regions between the heat conduction model (which does not include such physics) and the ice accretion model. Consequently, the convergence may not be assured.

5 Results and discussion

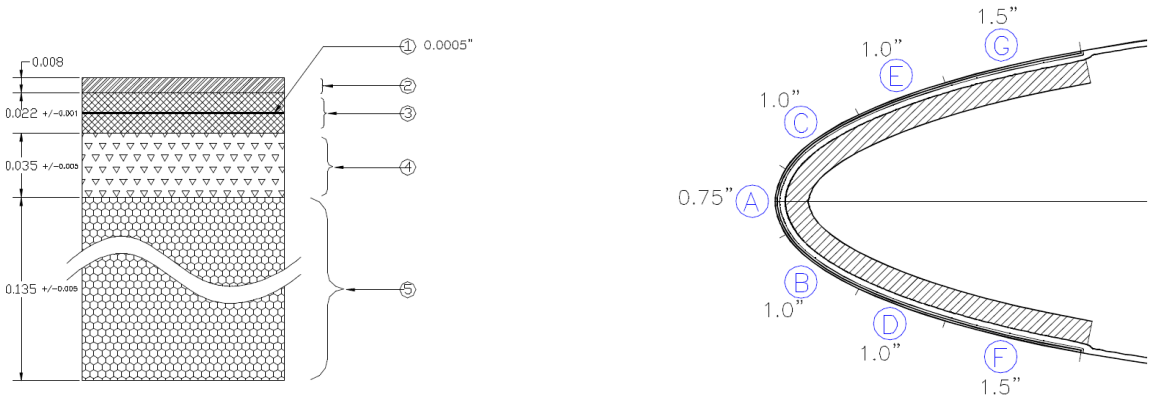

(a) Skin layers

(b) Pads layout

Figure 4: NACA 0012 skin structure (from ref. [1])

Test cases are selected from the paper published by Al-Khalil et al.[1]: both experimental and numerical results are reported for a NACA 0012 airfoil having a span length of 1.828 meters and a chord value of 0.9144 meters. Where available, results are also compared to the numerical analyses carried out by da Silva et al. [16] and by Bu et al. [2].

Both authors performed numerical studies of anti-icing systems using integral and differential boundary layer methods. As sketched in figure 4, the airfoil skin is composed of five material layers and is

Item	Material	Thermal conductivity K		Density, ρ		Specific heat, C_p		Thickness	
		btu/hr.ft.°F	W/m.°C	lbm/ft³	kg/m³	Btu/lbm.°F	J/kg.°C	inches	mm
1	Heating Element (alloy 90)	23.7	41.02	556	8906	0.092	385.2	0.0005	0.0127
2	Erosion Shield (SS 301 H)	9.4	16.27	501	8025	0.12	502.4	0.008	0.2032
3	Elastomer (Cox 4300)	0.148	0.26	86.4	1384	0.3 +/- 0.03	1256 +/- 125.6	0.022 +/- 0.001	0.559 +/- 0.0254
4	Fiberglass/Epoxy Composite	0.17	0.29	112	1794	0.375	1570.1	0.035 +/- 0.005	0.889 +/- 0.127
5	Silicone Foam Insulation	0.07	0.12	40.5	649	0.27 +/- 0.03	1130.4 +/- 125.6	0.135 +/- 0.005	3.429 +/- 0.127

Figure 5: Layer material properties

Table 1: Heaters setup

	Non-dimensional streawise distance s/c		*Anti-icing heat flux* [kW/m^2]			
Heater ID	*Start*	*End*	*22A*	*22B*	*67A*	*67B*
F	0.9178	0.9588	9.92	2.63	20.15	8.37
D	0.9588	0.9868	10.23	2.94	21.70	11.94
B	0.9868	1.0148	32.55	4.03	32.55	10.85
A	1.0148	1.0358	46.50	4.80	46.40	15.19
C	1.0358	1.0628	18.60	2.94	26.35	9.92
E	1.0628	1.0908	6.98	3.41	18.60	12.87
G	1.0908	1.1328	10.23	2.32	18.60	8.68

equipped with seven heating pads (from A to G), all located between the second and third layer starting from the external surface. Figure 5 summarizes the material properties of each layer.

The air flow and the collection efficiency have been computed with in-house solvers (respectively ZEN and Imp2D) on a three-level C-type structured mesh, having 98,000 quadrilateral cells in the finest level. The $y+$ on the airfoil surface ranges from 0.5 to 4. The $k-\omega$ TNT turbulence model by Kok et al. [9] is used.

The icing conditions are shown in table 2. Figure 6 compares the obtained collection efficiency with numerical results by Al-Khalil and Bu papers. The comparison with results by Bu is noticeable in both cases, while the ANTICE predictions result in a more smeared shape, as the impingement peak is slightly lower and the limits are larger. Obviously, the collection efficiency depends only on the icing

Table 2: Test cases icing conditions

Parameter	*Case 22*	*Case 67*
AOA [°]	0	00
V_∞ [m/s]	44.7	89.4
T_∞ [K]	265.5	251.4
LWC_∞ [Kg/m^3]	0.00078	0.00055
MVD_∞ [μm]	20	20

conditions and not on the heaters pad setup, hence evaporative and running wet cases will have the same β distribution if they have been conducted in the same icing conditions.

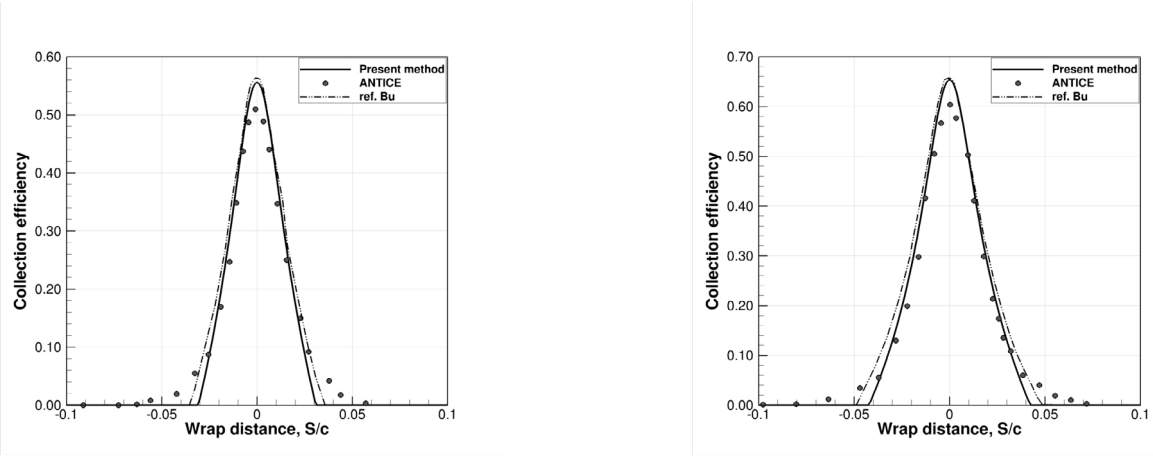

(a) Case 22

(b) Case 67

Figure 6: Collection efficiency compared with literature numerical results

Detailed information about the location and the power densities of the heaters are reported in table 1, where A and B refers to evaporative and running wet cases, respectively. Here s/c represents the non-dimensional wrap distance measured from the airfoil trailing edge in clockwise order. The wrap distance is the same as s/c but re-centered in the airfoil leading edge point. In the following, four cases will be presented, two in running-wet conditions (22B and 67B), two in evaporative mode (22A and 67A). For each condition, four types of output are proposed: the equilibrium surface temperature, the effective (or total) heat transfer coefficient, the runback mass flow rate (per unit span distance) and the mass balance contributions (mass flow rate per unit span distance). Following Al-Khalil observations, the laminar to turbulent transition has been numerically tripped at $s/c = 0.05$ in wrap distance along the airfoil surface in order to match the film coefficient distribution as observed from experimental data.

5.1 Running-wet cases

The running wet cases are referred to as 22B and 67B. For the former, only experimental and ANTICE code data by Al-Khalil [1] are available, for the latter numerical data by da Silva [16] and Bu [2] will be used in addition. Results and comparison plots are summarized in figure 7 and 8. In both cases, the agreement with surface temperature experimental data is quite satisfactory, especially around stagnation and in the outer regions, while some overshoots in the numerical prediction are observed in the middle. However, it can be noticed that such a feature is shared with both ANTICE code and reference data by da Silva and Bu, especially for case 67B. The temperature range is between the freezing point at 273.15 K and 282 K for case 22B and up to 300 K for case 67B.

The effective film coefficient h_{eff} is slightly underestimated by the present method, as observable from figures 7(b) and 8(b). In figure 7(b) it is also reported a comparison of the air-wall (dry conditions) heat transfer coefficient h_c computed with the present method and the ANTICE laminar prediction: the data are in good agreement, at least prior to the transition that has been artificially tripped in the CFD computation. This probably means that the underestimation in the total heat transfer coefficient is due to the presence of the surface water film. A possible answer is given in figures 7(c) and 8(c) where an overestimation of the runback mass flow rate is evident with respect to ANTICE predictions: indeed, for a given impingement mass flow rate, having more water flowing on the surface implies that less water has evaporated, which in turn implies a higher value of the local surface temperature (evaporative cooling is lower) and a lower effective heat transfer coefficient. The impingement, evaporative and freezing mass

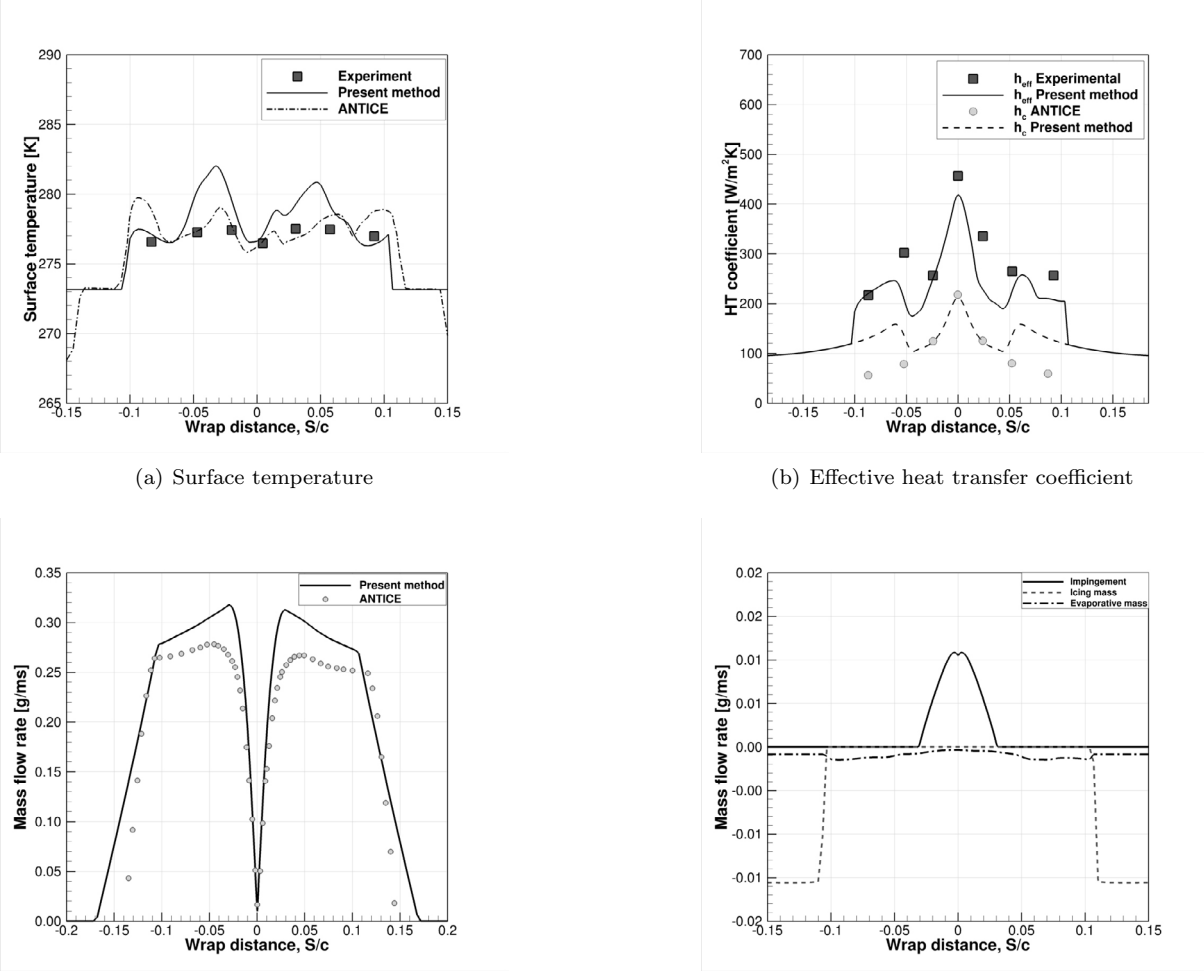

(a) Surface temperature

(b) Effective heat transfer coefficient

(c) Runback mass flux (Kg/ms)

(d) Mass balance contributions

Figure 7: Case 22B (running wet)

flow rates are plot in figures 7(d) and 8(d), where negative values indicate that mass is outgoing from the control volume. The evaporating mass is just a limited portion of the incoming mass due to relatively low surface temperature values; even a small runback ice formation is observed near the impingement limits, as also highlighted experimentally by Al-Khalil.

Figure 9 shows the skin temperature contour map as computed in the last coupled iteration together with the water droplet limiting trajectories and the runback ice formation. For the sake of clarity, the temperature contour levels below 273.15 K have been cut, so that it is easy to identify the freezing point. It can be observed that there are two peak regions in the temperature field close to the impingement limits and that the ice formation starts to grow near the location where the freezing point is met. The ice thickness for case 67B is bigger and less spread than case 22B despite of the noticeably higher heating power: this is explained by two main effects, first the larger impinging mass for case 67B, second, due to lower temperatures, the larger area (even beyond the protected region) covered by water runback for case 22B.

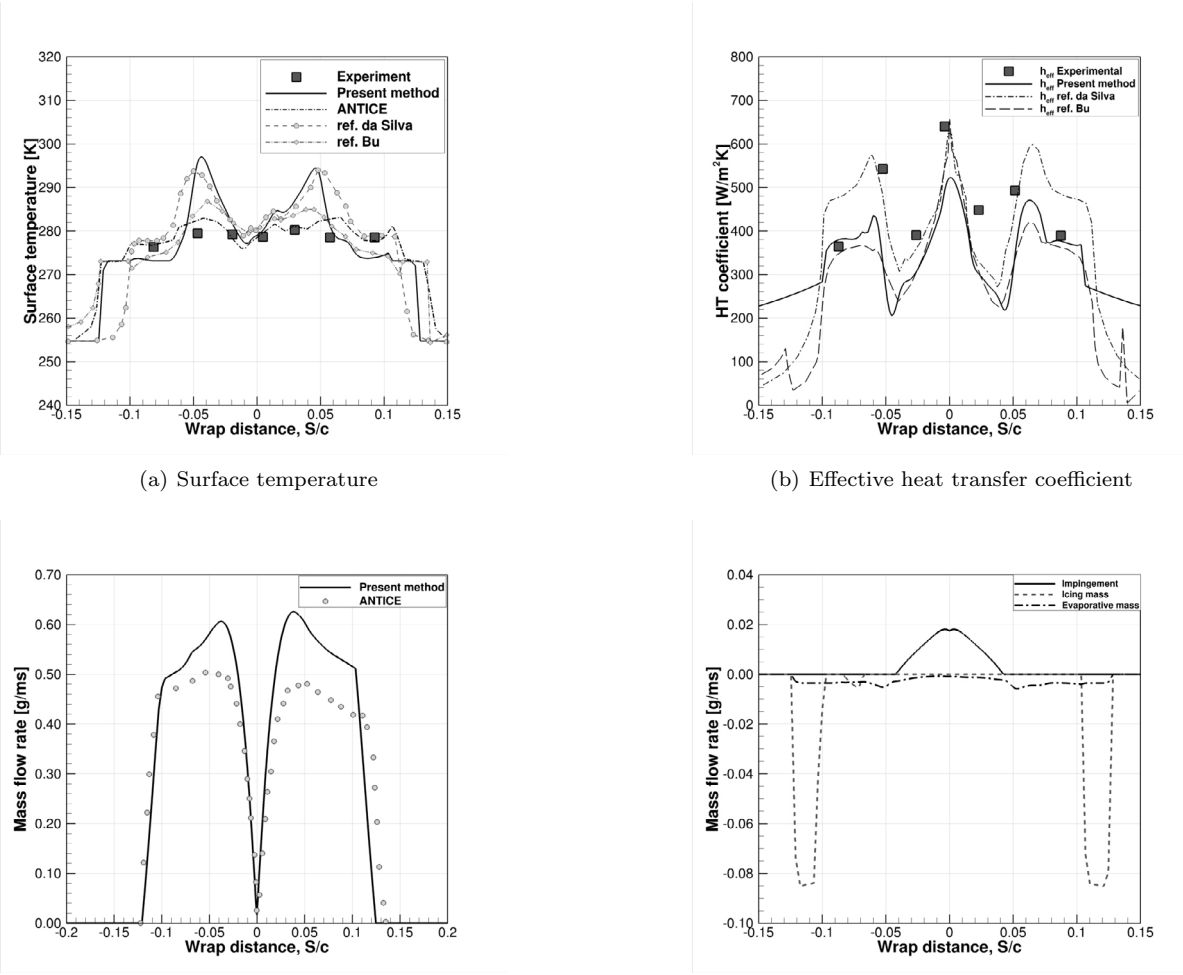

(a) Surface temperature

(b) Effective heat transfer coefficient

(c) Runback mass flux (Kg/ms)

(d) Mass balance contributions

Figure 8: Case 67B (running wet)

5.2 Evaporative cases

The evaporative cases are referred to as 22A and 67A. For both cases, reference data by Al-Khakil, da Silva and Bu are available. Results and comparison plots are summarized in figure 10 and 11. For case 22A, the predicted surface temperature shows a good agreement with the experiment throughout the whole heated region. The effective film coefficient is still underestimated as figure 10(b) indicates, however the trend in the laminar-turbulent transitional area is well captured. Due to high heater power values in combination with low impinging mass, this case is very close to be considered an actual fully evaporative case, as the runback mass in the impinging area is very limited (figure 10(c)) and the most of the impinging water evaporates in the wetted area (figure 10(d)).

Case 67A presents some discrepancies in the surface temperature profile past the impingement limits, where the value of the experiment thermocouple is significantly underestimated by both the present method and Bu's data. The effective film coefficient h_{eff} is still slightly underestimated, as reported in figure 11(b), but the discrepancy is here confined in a narrow region near the stagnation point, while the overall agreement is acceptable. Figures 11(c) provide a confirmation that the runback mass flow rate is

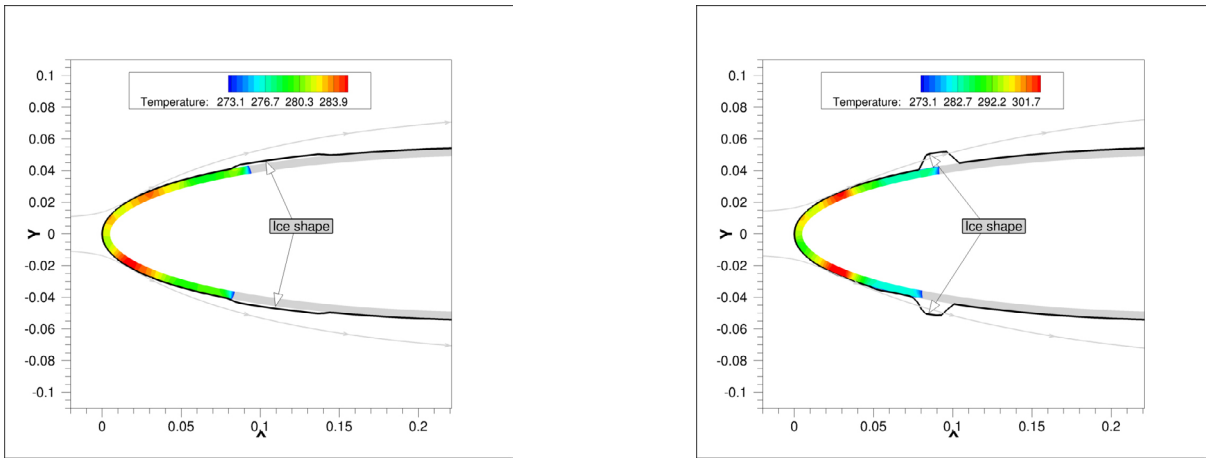

(a) Case 22B

(b) Case 67B

Figure 9: Skin temperature field with water droplet limiting trajectories and runback ice shape

overestimated with respect to Al-Khalil numerical predictions.

Unlike the previous case, the evaporating process does not manage to balance the larger incoming water mass (figure 11(d)), thus being of the same order of magnitude of case 22A. As a consequence, similar features to running-wet cases are observed, i.e. large amount of runback water and small ice formations at the extremes of the protected area. Indeed, figure 12 shows the skin temperature contour map as computed in the last coupled iteration together with the water droplet limiting trajectories and the runback ice formation. For case 22A, as already mentioned, no runback ice is present as the temperature is kept above the freezing point throughout the whole wet area and all the incoming mass is lost by evaporation. On the other hand, a very small triangle–shaped ice accretion is predicted by the present method as a result of some residual water mass flowing downstream and freezing immediately behind the protected area.

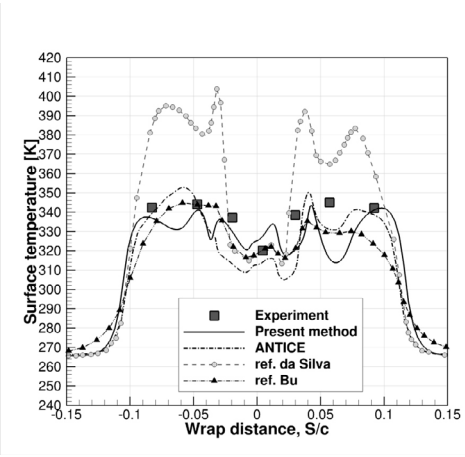

(a) Surface temperature

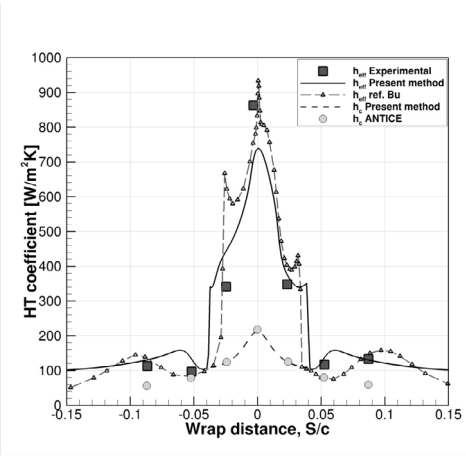

(b) Effective heat transfer coefficient

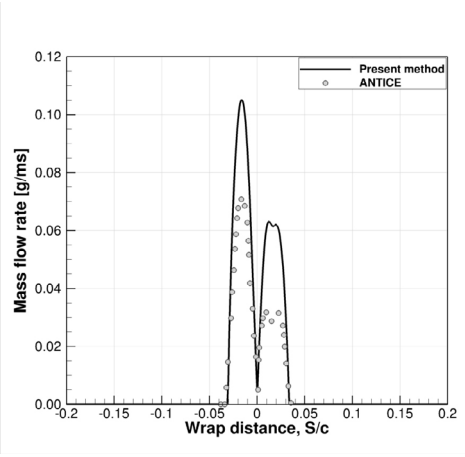

(c) Runback mass flux (Kg/ms)

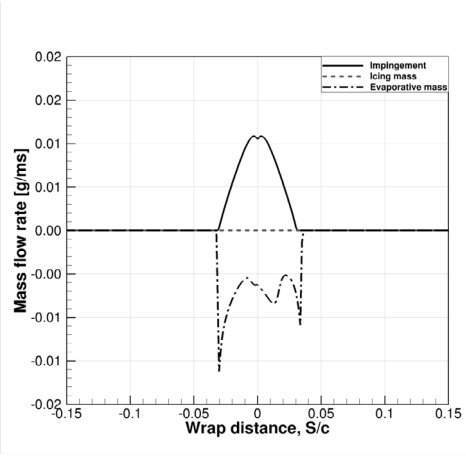

(d) Mass balance contributions

Figure 10: Case 22A (evaporative)

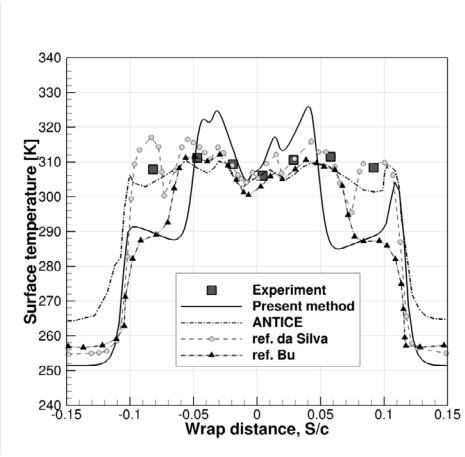

(a) Surface temperature

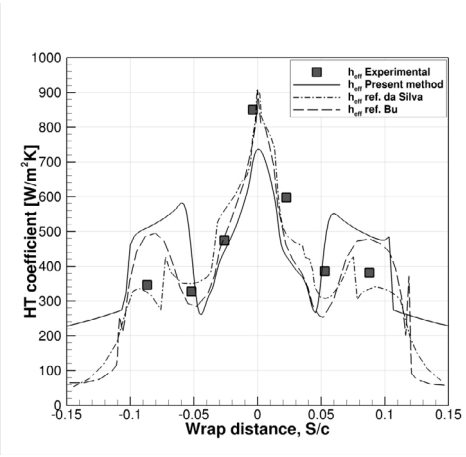

(b) Effective heat transfer coefficient

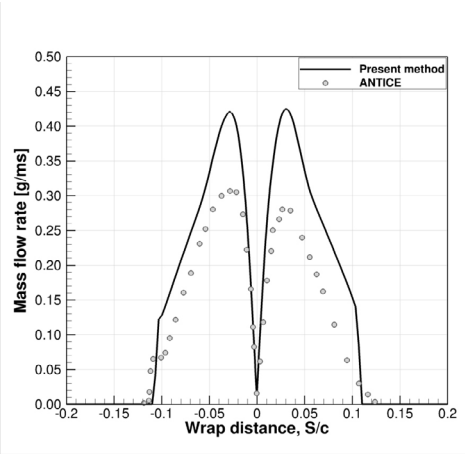

(c) Runback mass flux (Kg/ms)

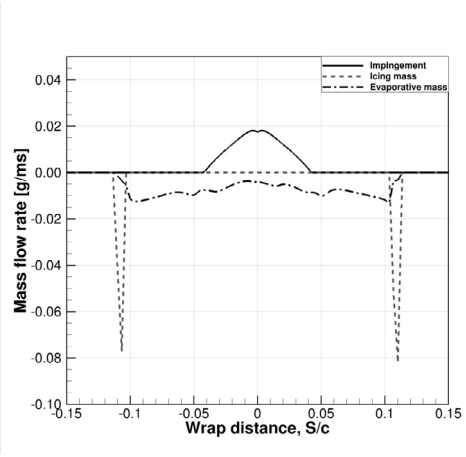

(d) Mass balance contributions

Figure 11: Case 67A (evaporative)

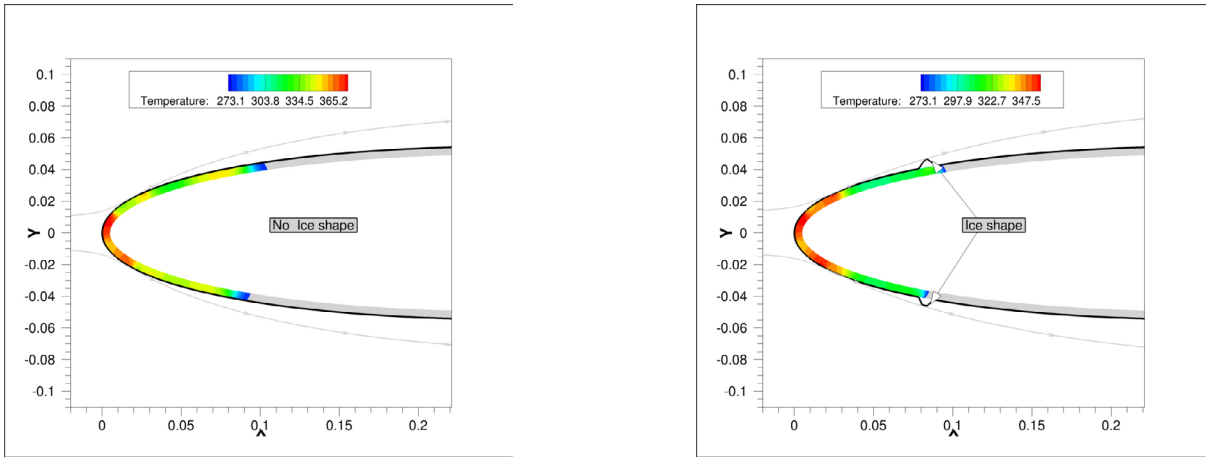

(a) Case 22A

(b) Case 67A

Figure 12: Skin temperature field with water droplet limiting trajectories and runback ice shape

Conclusions

A coupled approach has been presented and tested to numerically simulate anti-icing problems on airfoil shapes. It combines a classical Messinger-based ice accretion simulation with a FEM analysis for solving the heat conduction problem through the airfoil skin. The air flow and the local collection efficiency are evaluated by means of the finite volume method implemented within in-house solvers. In particular, the water droplet flow field is computed in every location of the solution domain by means of a Eulerian approach.

The coupling between the surface mass and energy equations and the heat conduction problem has been realized iteratively by searching for the convergence of the effective film coefficient distribution. Typically, three to five iterations are required to reach the convergence on the L_2 or L_∞ norm.

Results show that a satisfactory agreement has been reached with experimental data and numerical results has been reached, especially in evaporative conditions, while some overshoots are still observed in running wet conditions. A consistent trend has been observed in underestimating the total heat transfer coefficient and overestimating the runback mass flux with respect to ANTICE code by NASA: this can be probably due to the differences outlined in the impinging mass flux more than in the estimation of the evaporative rate. Further investigations will be devoted to extend the coupled code validation and to make comparative studies about the evaporative cooling law as applied to aircraft icing, as also recommended by Al-Khalil.

Electrothermal de-icing cases will be also considered even if no coupling with the external solution is needed.

Finally, the coupled approach has been designed and implemented in a fully parametric mode where the location, extension and power of the heaters can be easily changed. This is of fundamental importance towards the design of electro-thermal anti-icing systems, e.g. by numerical optimization aimed at minimizing the overall power required by the anti-icing system while keeping the surface clear of ice.

REFERENCES

[1] Kamel Al-Khalil, Charles Horvath, Dean Miller, William Wright, Kamel Al-Khalil, Charles Horvath, Dean Miller, and William Wright. Validation of NASA thermal ice protection computer codes. III - the validation of ANTICE. In *35th Aerospace Sciences Meeting and Exhibit*, number AIAA 97-0051. AIAA, American Institute of Aeronautics and Astronautics (AIAA), jan 1997.

[2] Xueqin Bu, Guiping Lin, Jia Yu, Shenghua Yang, and Xin Song. Numerical simulation of an airfoil electrothermal anti-icing system. *Proceedings of the Institution of Mechanical Engineers, Part G: Journal of Aerospace Engineering*, 227(10):1608–1622, 2013.

[3] Pietro Catalano and Marcello Amato. An evaluation of rans turbulence modelling for aerodynamic applications. *Aerospace Science and Technology*, 7:493–509, 2003.

[4] RW Gent, NP Dart, and JT Cansdale. Aircraft icing. *Philosophical Transactions of the Royal Society of London A: Mathematical, Physical and Engineering Sciences*, 358(1776):2873–2911, 2000.

[5] Frank P Incropera and David P De Witt. Fundamentals of heat and mass transfer. 1985.

[6] E Iuliano, G Mingione, F Petrosino, and F Hervy. Eulerian modeling of large droplet physics toward realistic aircraft icing simulation. *Journal of Aircraft*, 48(5):1621–1632, 2011.

[7] Emiliano Iuliano, Vincenzo Brandi, Giuseppe Mingione, Carlo de Nicola, and Renato Tognaccini. Water impingement prediction on multi-element airfoils by means of eulerian and lagrangian approach with viscous and inviscid air flow. In *44th AIAA Aerospace Sciences Meeting and Exhibit*, page 1270, 2006.

[8] Emiliano Iuliano, Giuseppe Mingione, Francesco De Domenico, and Carlo de Nicola. An eulerian approach to three-dimensional droplet impingement simulation in icing environment. In *AIAA Atmospheric and Space Environments Conference*, page 7677, 2010.

[9] Johan C Kok. Resolving the dependence on freestream values for the k-Ω turbulence model. *AIAA Journal*, 38(7):1292–1295, July 2000.

[10] Chao Ma, Yi Hua Cao, and Xin Xing Chu. Ice shape prediction based on an improved thermodynamic model. In *Applied Mechanics and Materials*, volume 192, pages 63–67. Trans Tech Publ, 2012.

[11] Erdogan Madenci and Ibrahim Guven. *The Finite Element Method and Applications in Engineering Using ANSYS®*. Springer-Verlag New York, Inc., Secaucus, NJ, USA, 2007.

[12] Konstanty C. Masiulaniec and William B. Wright. User's manual for the nasa lewis ice accretion/heat transfer prediction code with electrothermal deicer input. Technical Report NASA-CR-4530, NASA, 1994.

[13] Bernard L Messinger. Equilibrium temperature of an unheated icing surface as a function of air speed. *Journal of the Aeronautical Sciences*, 1953.

[14] T.G. Myers and D.W. Hammond. Ice and water film growth from incoming supercooled droplets. *International Journal of Heat and Mass Transfer*, 42(12):2233 – 2242, 1999.

[15] M. Necati OzisiK. *Heat conduction*. John Wiley and sons, second edition edition, 1993.

[16] Guilherme Silva, Otavio Silvares, Euryale Zerbini, Hamid Hefazi, Hsun-Hu Chen, and Kalle Kaups. Differential boundary-layer analysis and runback water flow model applied to flow around airfoils with thermal anti-ice. In *1st AIAA Atmospheric and Space Environments Conference*. American Institute of Aeronautics and Astronautics (AIAA), jun 2009.